The Astrophysical Journal Supplement Series, 282:49 (12pp), 2026 February https://doi.org/10.3847/1538-4365/ae2d08


# Assessing the Effects of Composition and Surface Roughness on the Photopolarimetric Response of Planetary Regoliths

Francisco J. García-Izquierdo[1], Elisa Frattin[1], Julia Martikainen[1,2,3], Olga Muñoz[1], Alvaro Alvarez-Candal[1], Fernando Moreno[1], María Passas-Varo[1], Juan Carlos Gómez-Martín[1], Teresa Jardiel[4], Marco Peiteado[4], Amador C. Caballero[4], Gorden Videen[5,6], Johannes Markkanen[7], Antti Penttilä[8], and Karri Muinonen[8]
[1] Instituto de Astrofísica de Andalucía, Glorieta de la Astronomía, 18008, Granada, Spain; fgarcia@iaa.es
[2] Instituto de Astrofísica de Canarias, 38200, La Laguna, Tenerife, Spain
[3] Nordic Optical Telescope, Rambla José Ana Fernández Pérez 7, 38711, Breña Baja, Spain
[4] Department of Electroceramics, Instituto de Cerámica y Vidrio (ICV), CSIC, C/Kelsen 5, 28049, Madrid, Spain
[5] Space Science Institute, 4750 Walnut Street, Suite 205, Boulder, CO 80301, USA
[6] Kyung Hee University, Yongin, Republic of Korea
[7] Institut for Geophysik und Extraterrestrische Physik, Technische Universität Braunschweig, Mendelssohnstr. 3, 38106 Braunschweig, Germany
[8] Department of Physics, PO Box 64, FI-00014, University of Helsinki, Helsinki, Finland
*Received 2025 October 10; revised 2025 December 9; accepted 2025 December 11; published 2026 January 27*

## Abstract

This study is part of an ongoing project in which we experimentally examine the effect of composition (refractive index) and surface roughness on the scattering matrix elements of a set of well-characterized rough regolith simulants. A set of four cylindrical Mars regolith simulants with controlled degrees of porosity and surface roughness is studied. Photopolarimetric measurements, spanning scattering angles from 94 to 177 , were conducted at a wavelength of 488 nm at the Instituto de Astrofísica de Andalucía Cosmic Dust Laboratory. These results are compared with those previously obtained at 640 nm. The higher absorption of the Mars simulants at 488 nm compared to 640 nm produces a significant effect on all elements of the scattering matrix. The trends previously observed in the diagonal elements of the scattering matrix and in the albedo as a function of surface roughness remain unaffected by the differences in refractive indices at both wavelengths. The comparison with the previous study enables the investigation of sample reddening across the scattering-angle range, with a trend also observed between surface roughness and reddening. Moreover, within our measured angular range, the effect of absorption is consistent with Umov's law, whereas the effects of surface roughness do not appear to support its validity. Nearly all samples exhibit a shallow negative polarization branch.

*Unified Astronomy Thesaurus concepts:* Regolith (2294); Planetary surfaces (2113); Polarimetry (1278); Optical constants (Dust) (2270)

## 1. Introduction

*Regolith* is the unconsolidated material of varying morphology, particle size, and chemical composition that covers the surfaces of astronomical objects such as terrestrial planets, natural satellites, and asteroids. Research on regolith remains an open and active field in astrophysics, where the study of its scattering behavior plays a crucial role. Photometric and polarimetric observations of regolith-covered surfaces can reveal physical properties such as roughness, porosity, composition, size distribution, and degree of compaction.

Ground-based and spacecraft observations have yielded intensity and polarimetric features in the angular distributions of the scattered flux for a wide variety of targets. These are known as the intensity and polarization phase function. The polarization phase function can have both negative and positive branches, and the inversion angle is the phase angle at which the polarization changes signs. In A. Cellino et al. (2005), the inversion angle was determined for near-Earth objects from UBVRI phase-polarization measurements. In S. Fornasier et al. (2006), through the Asiago Cima Ekar survey, polarization phase curves were produced for 36 asteroids at phase angles near the backscatter region. S. Bagnulo et al. (2015) identified distinct polarimetric trends among asteroid taxonomic families. Building on this work, I. Belskaya et al. (2017) incorporated new observations with existing data to refine polarimetric features for 283 asteroids, revealing consistent patterns across taxonomic classes. A recent review on polarimetry of solar system minor bodies is presented by S. Bagnulo et al. (2025). Furthermore, spectroscopic phase reddening, which refers to the increase in reflectance with wavelength becoming steeper at larger phase angles, has been widely documented for several targets, highlighting the diagnostic power of phase-angle-dependent observations. S. Fornasier et al. (2020) measured clear reddening on Bennu over a wide range of phase angles using the OVIRS instrument from the OSIRIS-REx mission. E. Tatsumi et al. (2020) observed similar reddening on Ryugu using data from the Telescopic Optical Navigation Camera on board the Hayabusa2 spacecraft. Ground-based observations studied by J. A. Sanchez et al. (2012) for a dozen near-Earth asteroids also revealed pronounced reddening.

Laboratory experiments and numerical modeling help separate how different physical properties affect scattering behavior, making observational data easier to understand. Numerous laboratory experiments have been conducted to investigate how sample properties influence the phase function and the degree of linear polarization (DLP) of clouds of dust particles (Y. Shkuratov et al. 2006; E. Hadamcik et al. 2011;

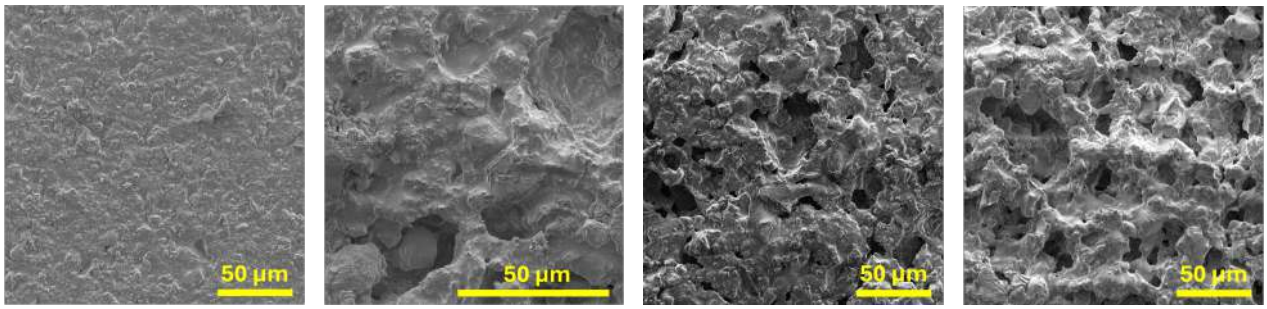


(a) MASC-1 (b) MASC-2 (c) MASC-3 (d) MASC-4

**Figure 1.** SEM images of the samples MASC-1 (a), MASC-2 (b), MASC-3 (c), and MASC-4 (d). The yellow bar indicates 50 $\mu$m.

E. Frattin et al. 2019, 2022; J. C. Gómez-Martín et al. 2023) and/or regolith analogs (R. M. Nelson et al. 2018; S. Spadaccia et al. 2022; E. Frattin et al. 2025). Additional experiments have examined the scattering behavior of icy deposits on regolith (O. Poch et al. 2018; S. Spadaccia et al. 2023). In parallel, numerical simulations using radiative transfer and coherent backscattering models have reproduced key optical features of particulate media, such as the negative polarization branch (NPB), in both low and moderate density regimes (K. Muinonen et al. 2012, 2018; A. Penttilä et al. 2021). Recent developments have extended these models to denser and more complex media, including nonspherical particles and close-packed geometries (D. Stankevich et al. 2023; J. Markkanen & A. Penttilä 2023; K. Muinonen et al. 2025).

Several studies of the properties of cosmic dust using analog samples and photopolarimetry have been conducted at the Instituto de Astrofísica de Andalucía Cosmic Dust Laboratory (IAA-CODULAB; O. Muñoz et al. 2010, 2011). Additionally, the Granada-Amsterdam Light Scattering Database (O. Muñoz et al. 2025) contains all datasets obtained by CODULAB, including experimental light-scattering Mueller matrices and sample properties such as complex refractive indices, size distributions, and images. This work is part of an ongoing project aimed at disentangling the effects of surface roughness, porosity, and chemical composition on the scattering patterns of regolith simulants. In particular, we focus here on the effects of composition and surface roughness.

We investigate the impact of chemical composition on light absorption through the imaginary part of the complex refractive index, as well as the effect of surface roughness on the light-scattering Mueller matrix. We study a set of four centimeter-sized, regolith analogs composed of well-characterized Martian analog dust powder, previously used by E. Frattin et al. (2025). Measurements were performed over a scattering angle range from 94 to 177 at a wavelength of 488 nm. This paper is structured as follows: Section 2 provides a brief description of the samples, while Section 3 outlines the experimental setup and theoretical framework. Section 4 presents the experimental measurements and results. In Section 5, we discuss the findings within an astronomical context, and Section 6 concludes with a summary of the work.

## 2. Sample Description

The regolith simulants Martian Analogue Synthesized Cylinder 1 (MASC-1) through MASC-4, previously characterized by E. Frattin et al. (2025), consist of cylindrical samples with radius × height dimensions of 0.2 × 0.4 cm. The cylindrical simulants are produced by sintering Mojave Mars Simulant 2 (MMS2) powder at the Instituto de Cerámica y Vidrio. This powder has a size distribution with an effective radius $r_{\text{eff}} = 1.25\,\mu$m and effective variance $v_{\text{eff}} = 1.37$, as defined by J. E. Hansen & L. D. Travis (1974), after several stages of milling and sieving. The complex refractive index of MMS2 powder is $m = 1.5 + i0.00035$ at a wavelength of 640 nm and $m = 1.5 + i0.0011$ at a wavelength of 488 nm (J. Martikainen et al. 2023, 2025). To obtain porosity, the powder is mixed with a volatile organic, whose proportion controls the degree of porosity. The volatile organic is removed with heat leaving pores. Further details of the production process can be found in E. Frattin et al. (2025).

To characterize the surface roughness, we obtained scanning electron microscopy (SEM) images of one of the two parallel circular bases of the cylindrical regolith analogs (Figure 1). The SEM images reveal the surface structures, where darker areas correspond to deeper regions. Surface roughness increases progressively from MASC-1 (Figure 1(a)) to MASC-4 (Figure 1(d)). SEM images of MASC-1, MASC-3, and MASC-4 (Figures 1(a), (b), and (d)) cover an area of 200 × 200 $\mu$m$^2$, whereas the SEM image of MASC-2 (Figure 1(b)) covers an area of 100 × 100 $\mu$m$^2$. SEM images at the same lower magnification for the samples are shown in E. Frattin et al. (2025). Moreover, we performed atomic force microscopy (AFM) analysis to estimate surface roughness at smaller scales. With this technique, sample topography is captured by scanning the surface with an oscillating cantilever, where changes in tip–sample interaction forces are tracked via oscillation amplitude. Scan time was fixed at 10 minutes for all measurements. For a constant scan duration, more topographically complex regions can lead to obtaining smaller imaged areas due to the need for denser spatial sampling (further details in E. Frattin et al. 2025). In Figure 2, we present AFM height maps corresponding to our four regolith analog samples. The parameter used to estimate surface roughness is the arithmetic average height parameter, $S_a$, which is the average absolute deviation of irregularities from the mean line over a sampling length (E. S. Gadelmawla et al. 2002). Table 1 summarizes the $S_a$ values and their corresponding scanned areas, measured over three distinct patches per sample.

## 3. Experimental Setup

The experimental measurements have been conducted at the CODULAB located at the IAA (O. Muñoz et al. 2010). This instrument is designed to measure the scattering matrices of various types of samples, including clouds of micron-sized particles (E. Frattin et al. 2019; J. C. Gómez-Martín et al. 2021; O. Muñoz et al. 2021), single millimeter-sized pebbles

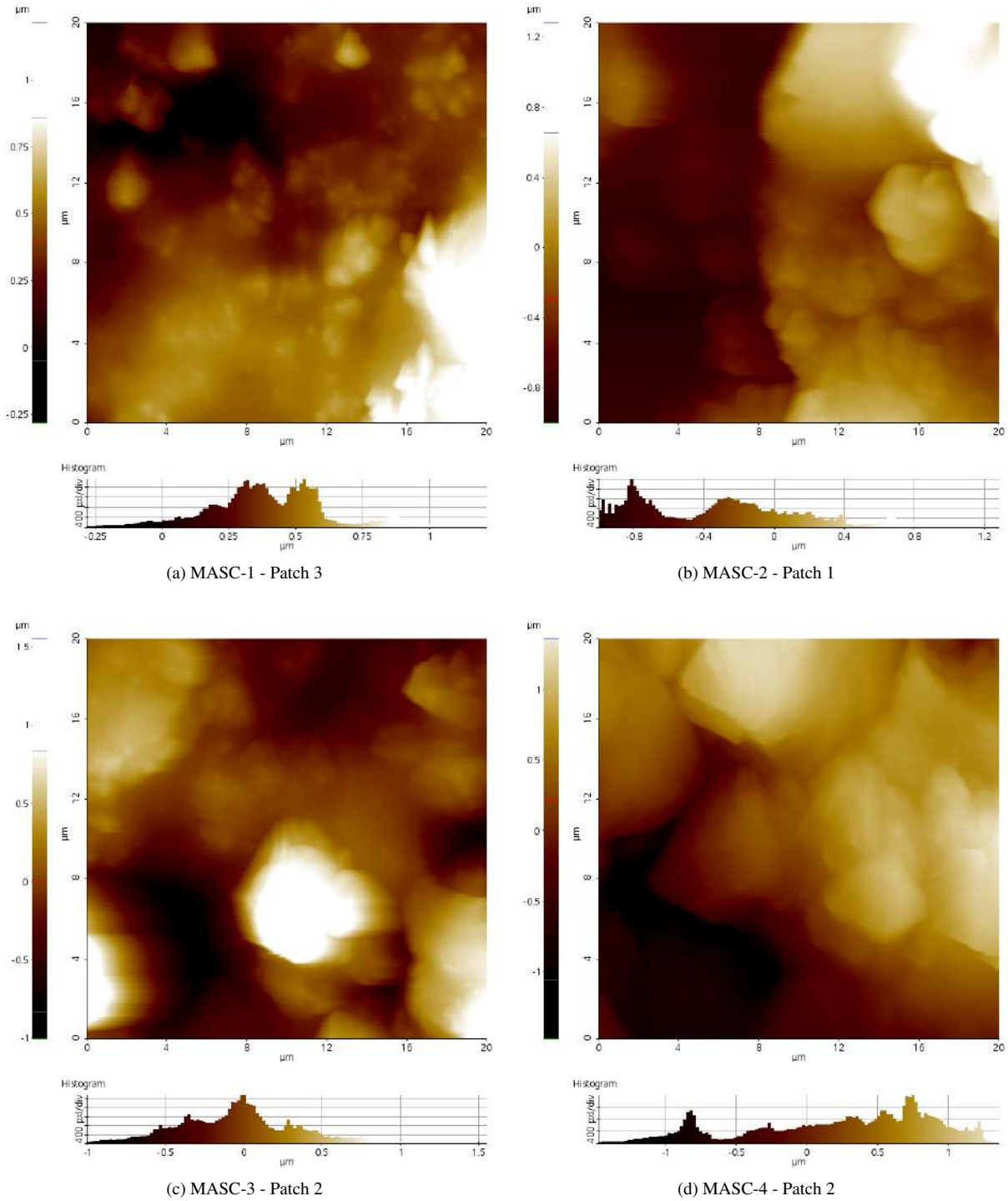


(a) MASC-1 - Patch 3

(b) MASC-2 - Patch 1

(c) MASC-3 - Patch 2

(d) MASC-4 - Patch 2

**Figure 2.** AFM color maps of the MASC-1 (a), MASC-2 (b), MASC-3 (c), and MASC-4 (d) samples. The color bar to the left of each color map indicates the depth scale (in microns). The histograms at the bottom of each color map indicate the pixel counts over the absolute variation depth (in microns). The images cover an area of $20 \times 20\ \mu m^2$.

(O. Muñoz et al. 2020; E. Frattin et al. 2022), and regolith analog surfaces (E. Frattin et al. 2025). For the measurements presented in this work, the optical setup of CODULAB was adapted as shown in Figure 3, see also E. Frattin et al. (2025). The laser source is a Coherent High Performance OBIS™, which emits at 488 nm. A computer-controlled filter wheel (FW) with gray filters of varying density placed between the laser and the polarizer (*P*) to scale the laser beam flux for each scattering angle. The laser beam passes through a polarizer (*P*) and then through an electro-optic modulator (*M*). After the modulator, a beam expander widens the laser beam and provides illumination over large areas of the samples. A diaphragm (*D*) is used to adjust the size of the laser beam spot. The cylindrical sample is placed on a conical-tip flat black holder. To ensure the surface of interest is centered within the ring, the holder is mounted on an *x*–*y*–*z* rotational stage.

The laser beam illuminates the flat, circular base of the cylindrical analogs at normal incidence, as shown in Figure 3.

**Table 1**
Measured Average Height Surface Roughness Parameter ($S_a$ in $\mu$m) and Corresponding Scanned Area (in $\mu m^2$) for the Three Patches Analyzed for Each Sample by AFM Analysis

| | | Patch | | |
|---|---|---|---|---|
| | | 1 | 2 | 3 |
| MASC-1 | $S_a$ ($\mu$m) | 0.2809 | 0.4600 | 0.4115 |
| | Area ($\mu m^2$) | 400 | 400 | 400 |
| MASC-2 | $S_a$ ($\mu$m) | 0.4746 | 0.9428 | 0.3122 |
| | Area ($\mu m^2$) | 400 | 900 | 400 |
| MASC-3 | $S_a$ ($\mu$m) | 0.5122 | 0.3214 | 0.8206 |
| | Area ($\mu m^2$) | 400 | 400 | 400 |
| MASC-4 | $S_a$ ($\mu$m) | 1.8804 | 0.6037 | 0.4014 |
| | Area ($\mu m^2$) | 225 | 400 | 400 |

**Note.** Table adapted from E. Frattin et al. (2025).

The scattered light is then collected by a photomultiplier (PM) tube detector that moves along a ring with a diameter of one meter. The modulated scattered signal at the PM detector is split into DC and AC components using low-pass and bandpass filters. Lock-in amplifiers produce continuous signals $S(\theta)$ and $C(\theta)$, where contributions from signals other than the reference frequencies $\omega$ and $2\omega$ are attenuated to near zero. We refer the reader to O. Muñoz et al. (2010) for further details. An additional PM tube, serving as a PM monitor, is fixed in position at 100 of the scattering angle. The PM monitor compensates for intensity variations caused by the FW. In these experiments, the cylinders are sufficiently long to prevent light transmission through the sample, ensuring that light scattering occurs only in the upper layers. The range of scattering angles $\theta$ is constrained from 90 to 177 . However, due to shadowing effects, an acceptable signal-to-noise ratio is achieved from 94 onward. In addition to the modulation of the incident light, lock-in detection combined with the use of optical elements such as an analyzer and a quarter-wave plate ($A$ and $Q$, respectively) on the PM detector allows for the measurement of the full light-scattering Mueller matrix for the samples.

This scattering matrix $F$ relates the Stokes vectors of the incident ($I_0$, $Q_0$, $U_0$, $V_0$) and the scattered ($I_S$, $Q_S$, $U_S$, $V_S$) light, as described by J. W. Hovenier et al. (2004). The scattering-matrix elements $F_{ij}$ depend on the wavelength of the incident light and on the properties of the samples. Moreover, the presence of symmetries in the samples can null certain matrix elements and impose relations among others, leading to a simplified form of the scattering matrix (H. C. van de Hulst 1981). In particular, for randomly oriented particles, mirror symmetry, and under the principle of electromagnetic reciprocity, only the diagonal elements $F_{11}$, $F_{22}$, $F_{33}$, and $F_{44}$ remain independent, while the off-diagonal elements satisfy the symmetry relations $F_{12} = F_{21}$ and $F_{34} = -F_{43}$, the rest being zero. Assuming these symmetries and under unpolarized incident light, the element $F_{11}(\theta)$ represents the scattered flux commonly known as the phase function. The ratio $-F_{12}(\theta)/F_{11}(\theta)$ gives the DLP under the same conditions. Both quantities are widely used in astronomical applications and can be obtained directly from observations. Astronomical observations typically express these quantities as a function of

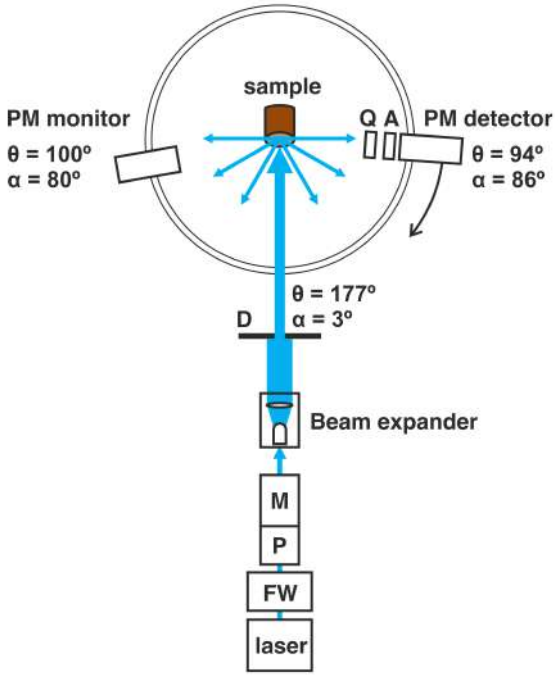


**Figure 3.** Schematic overview of the adapted CODULAB optical train as seen from above. FW = filter wheel, $P$ = polarizer, $M$ = modulator, $D$ = diaphragm, $A$ = analyzer, $Q$ = quarter-wave plate, and PM = photomultiplier. Relevant angular positions are detailed as scattering angle ($\theta$) and as phase angle ($\alpha$).

the phase angle, defined as $\alpha = 180 - \theta$. Moreover, the use of polarized light allows us to obtain the elements $F_{22}(\theta)/F_{11}(\theta)$ and $F_{33}(\theta)/F_{11}(\theta)$, both related to linear depolarization, $F_{44}(\theta)/F_{11}(\theta)$ related to circular depolarization, and $F_{34}(\theta)/F_{11}(\theta)$ related to linear-circular polarization coupling. The scattering-matrix formalism has been extensively studied, and detailed explanations can be found, for instance, in H. C. van de Hulst (1981) and J. W. Hovenier et al. (2004).

## 4. Results

The experimental scattering matrices as functions of scattering angle for the regolith simulants, at 488 nm, are presented in Figure 4. As mentioned, the measured scattering angle ranges from 94 to 177 , with measurements taken in steps of 2 from 94 to 150 , and in steps of 1 from 150 to 177 . This limitation in angular range is due to the use of normal incidence. As the incident light is fully absorbed within the sample without any transmitted radiation, scattering is predominantly confined to the surface region. This behavior supports the assumption of a semi-infinite medium. The measurement protocol is as follows: for each of the five optical configurations required to obtain the full scattering matrix, three measurement runs were performed. In each run, the samples were removed and repositioned on the holder to minimize the influence of positioning on the measured scattering-matrix elements. The results shown in Figure 4 represent the averages of the three runs. For some data points, the marker size exceeds the length of the error bars. The larger error bars observed at angles up to approximately 110 are due to the lower signal-to-noise ratio, resulting from light absorption at 488 nm and from shadowing effects caused by surface irregularities.

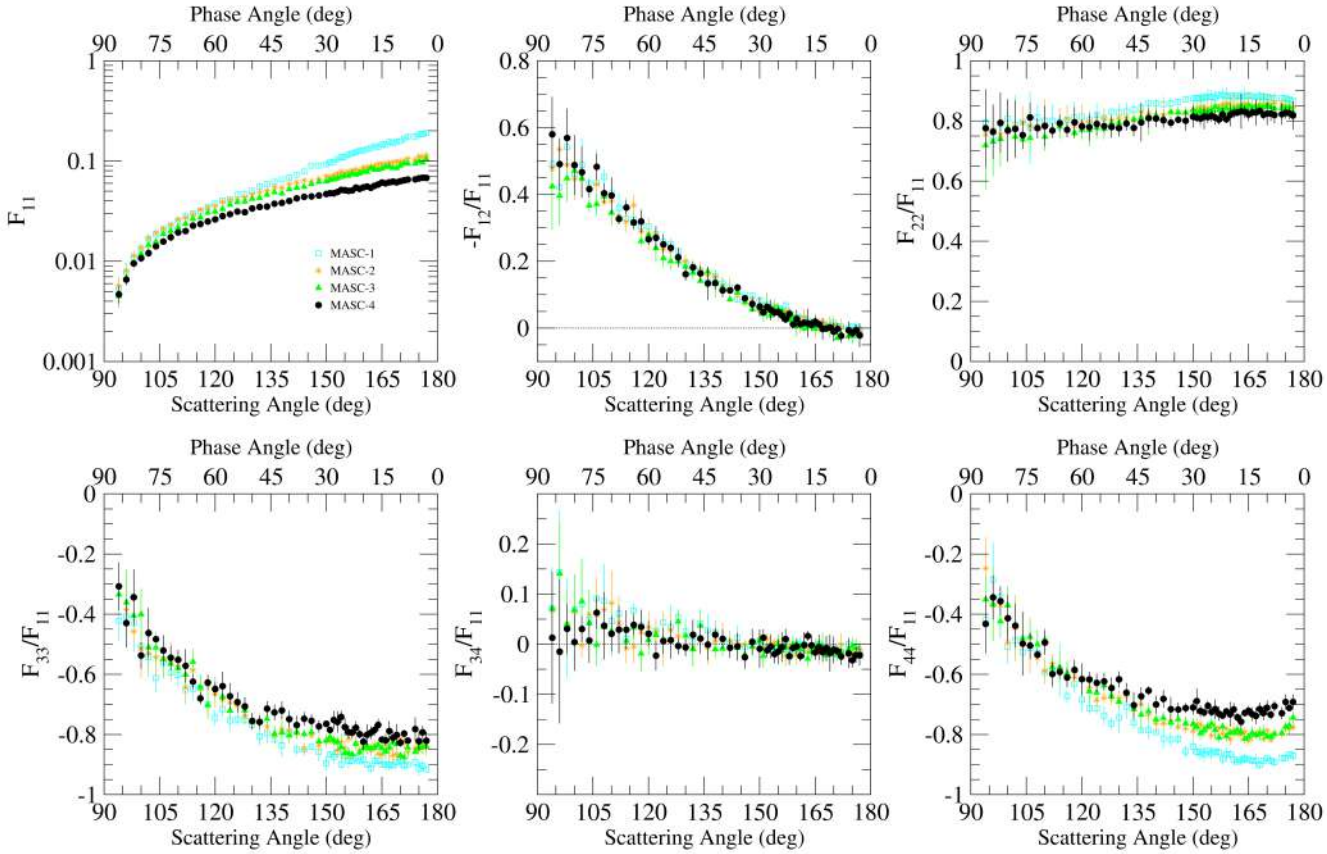


**Figure 4.** Experimental scattering-matrix elements as functions of the scattering (phase) angle, $\theta$ ($\alpha$), for MASC-1 (cyan empty squares), MASC-2 (orange stars), MASC-3 (green triangles), and MASC-4 (black circles). The wavelength is 488 nm.

Figures 5 and 6 compare the measured scattering-matrix elements at 488 nm (blue circles) with those obtained by E. Frattin et al. (2025) at 640 nm (red squares) for samples MASC-1 and MASC-4, respectively. The measured values of $F_{13}(\theta)/F_{11}(\theta)$, $F_{14}(\theta)/F_{11}(\theta)$, $F_{24}(\theta)/F_{11}(\theta)$, $F_{31}(\theta)/F_{11}(\theta)$, and $F_{41}(\theta)/F_{11}(\theta)$ (Figure A1 in the Appendix) are found to be zero within their error bars over the measured scattering angle range. We do not show the wavelength dependence for the other samples, as they exhibit similar behavior. These results demonstrate the effect of stronger absorption at shorter wavelengths, consistent with the wavelength dependence of the MMS2 refractive index.

### 4.1. Phase Function

The phase-function curves of the samples are plotted in logarithmic scale in the upper-left panel of Figure 4. These measured values are normalized to $F_{11}(170\ )$, and then multiplied by their albedos values at 170 . Due to instrumental limitations, obtaining geometric albedo at 180 is not possible; therefore, we use the value at 170 as a proxy. To obtain this value, a Spectralon target is used as a reference. The Spectralon (Labsphere SRT-99-020 AA-00823-000) is an approximately Lambertian surface made of a fluoropolymer with a nominal reflectance of 99%. The procedure consists of comparing the signals received at 170 under identical conditions between the samples and the Spectralon. Then, the geometric albedo is computed as $A(170°) = F_{11}^{M}(170°)/F_{11}^{S}(170°)$, where $F_{11}^{M}(170°)$ and $F_{11}^{S}(170°)$ are the phase-function values at 170 for the samples and the Spectralon, respectively. The results for the albedo at 170 at 488 nm are summarized in Table 2, along with the values obtained at 640 nm by E. Frattin et al. (2025). Among the samples, MASC-1 is the brightest with an albedo at 488 nm of 16%, followed by MASC-2 with 10% and MASC-3 with 9%. MASC-4 is the darkest sample with an albedo of 6%. As shown in Table 2, we find an inverse relationship between albedo and surface roughness. This trend is consistent in both wavelengths, 488 and 640 nm. Our experimental data also show an inverse relationship between albedo and the imaginary part of the refractive index. As shown in the upper-left panels in Figures 5 and 6, this relation holds across the entire measured scattering angle range; that is, the higher absorption at 488 nm produces a significantly darker phase function. The stronger absorption in the blue compared to the red explains the reddish-brown color of our samples. The effect of refractive index on albedo is stronger than that of surface roughness.

### 4.2. DLP

The DLP, defined as $-F_{12}(\theta)/F_{11}(\theta)$, is shown in the upper-middle panel of Figure 4 for the four samples at 488 nm. In the interval from 94 to 105 , error bars are larger than at angles beyond 105 . Within the measured angular range, the DLP curves tend to decrease with increasing scattering angle. We do not observe significant differences in the DLP curves among the four samples at 488 nm, despite their varying degrees of surface roughness. The same panel of Figures 5 and 6 illustrates the effect of the imaginary part of the refractive index on the DLP curves for MASC-1 and MASC-4, respectively. The higher imaginary part of the refractive index

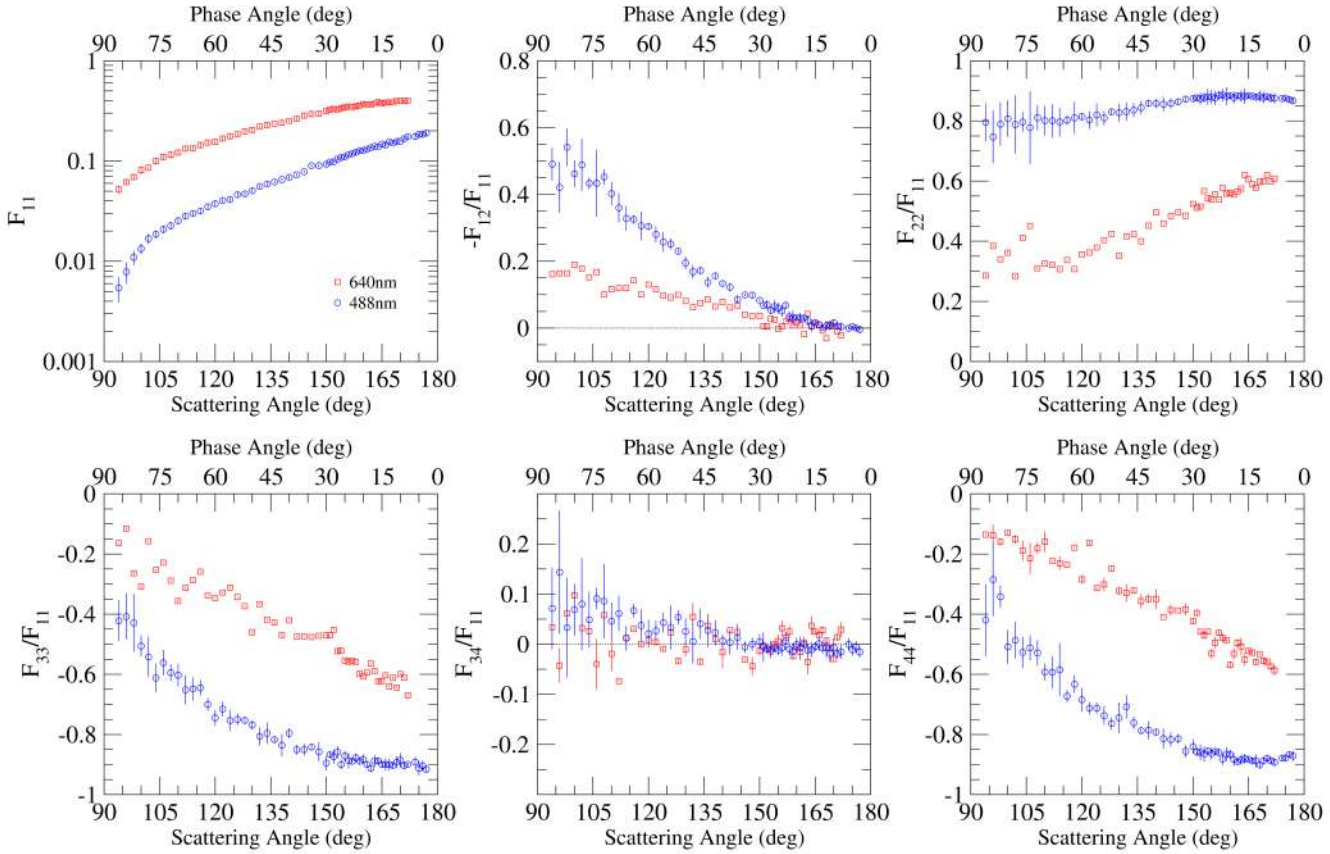


**Figure 5.** Experimental scattering-matrix elements as functions of the scattering (phase) angle, $\theta$ ($\alpha$), for MASC-1 at 640 nm (red squares; E. Frattin et al. 2025) and 488 nm (blue circles).

at 488 nm produces a significantly larger DLP at nearly all measured scattering angles.

The backscattering region deserves special attention. Figure 7 provides a magnification of the DLP curves in this region to highlight the NPB. The upper, middle, and bottom panels correspond to the DLP for the four regolith analog samples at 488 nm, and for MASC-1 and MASC-4 at both 488 and 640 nm, respectively. The NPB is a polarimetric feature produced by coherent backscattering and single-particle mechanisms that have been widely studied (A. A. Ovcharenko et al. 2006). It is typical of atmosphereless bodies (e.g., D. Kuroda et al. 2018; J. Geem et al. 2022) and cometary comae (W. Thompson 2015; E. Zubko et al. 2020). The upper panel of Figure 7 shows the effect of surface roughness at 488 nm. Surface roughness causes all samples to exhibit a very shallow NPB, with the two roughest samples (MASC-3 and MASC-4) showing a slightly deeper NPB. The depth and width of the NPB are influenced by multiple scattering and shadowing effects introduced by surface roughness. The middle and bottom panels of Figure 7 show the effect of wavelength on the NPB. To study this effect more clearly, three-point moving averages were calculated to smooth the data, resulting in the turquoise and magenta curves for 488 and 640 nm, respectively. In both cases, a higher imaginary part of the refractive index produces a slightly shallower NPB. For MASC-1, the smoothed data show that the NPB is absent at 488 nm, while it begins at 167 at 640 nm, with a maximum depth of $-0.9\%$. For MASC-4, the smoothed data show that the NPB begins at 168 at 488 nm and at 158 at 640 nm, with maximum depths of $-1.4\%$ and $-2.2\%$, respectively. The effect of absorption on the NPB appears small in our experiments, and the 640 nm data are quite scattered, suggesting that further studies are needed to clarify these trends.

### 4.3. Other Scattering-matrix Elements

The scattering-matrix elements $F_{22}(\theta)/F_{11}(\theta)$, $F_{33}(\theta)/F_{11}(\theta)$, and $F_{44}(\theta)/F_{11}(\theta)$ (upper-right, lower-left, and lower-right panels of Figure 4, respectively) display a dependence on the scattering angle over the angular range from 115 to 177 at 488 nm; however, it is not so strong as at 640 nm. For these matrix elements, the higher absorption at 488 nm reduces the effect of surface roughness. The increase of surface roughness yields lower absolute values for the $F_{33}(\theta)/F_{11}(\theta)$ and $F_{44}(\theta)/F_{11}(\theta)$ curves at nearly all measured scattering angles. By contrast, $F_{22}(\theta)/F_{11}(\theta)$ increases with decreasing surface roughness. As shown in Figures 5 and 6, the higher absorption at the blue wavelength produces a significant effect on the $F_{22}(\theta)/F_{11}(\theta)$, $F_{33}(\theta)/F_{11}(\theta)$, and $F_{44}(\theta)/F_{11}(\theta)$ matrix elements. The matrix element $F_{34}(\theta)/F_{11}(\theta)$ remains near zero at both wavelengths, and as in our previous work, no trends related to surface roughness are observed.

## 5. Astrophysical Implications

Several astronomical studies have investigated albedo, the phase function $F_{11}(\alpha)$, and the DLP, $-F_{12}(\alpha)/F_{11}(\alpha)$. These quantities can be directly measured by in situ and remote-sensing observations of solar system bodies (I. Belskaya & S. Bagnulo 2015; A. Cellino et al. 2015b; M. Ishiguro et al. 2017), and they

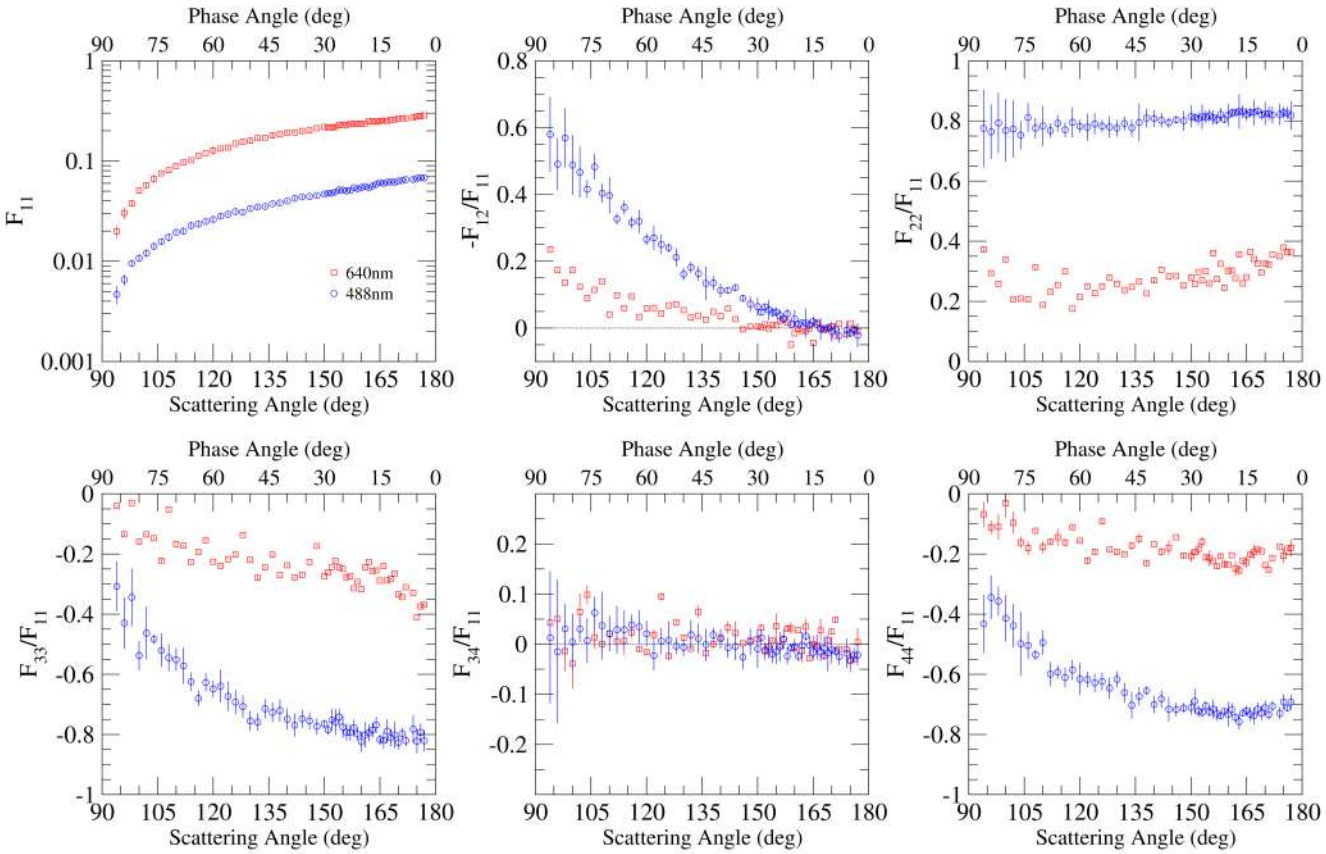


**Figure 6.** Experimental scattering-matrix elements as functions of the scattering (phase) angle, $\theta$ ($\alpha$), for MASC-4 at 640 nm (red squares; E. Frattin et al. 2025) and 488 nm (blue circles).

**Table 2**
Albedo $A$ at 170 of Scattering Angle in Percentage

| Samples | MASC-1 | MASC-2 | MASC-3 | MASC-4 |
|---|---|---|---|---|
| $A$ (%) (640 nm) | 40 4 | 32 3 | 32 4 | 27 2 |
| $A$ (%) (488 nm) | 16 4 | 10 2 | 9 2 | 6 1 |

**Note.** Data at 640 nm are from E. Frattin et al. (2025).

provide essential information for characterizing the physical properties of these bodies. For this reason, we analyze the astrophysical implications of our photopolarimetric results.

### 5.1. Planetary Albedo: Mars

A. Mallama (2007) retrieved albedo from Mars using the Solar and Heliospheric Observatory spacecraft, which is quite similar to what is shown in Table 2 at 488 nm and 10 phase angle (170 scattering angle). In that study, they used *U*, *B,* and *V* filters, with central wavelengths of 360, 440, and 550 nm, and full widths at half maxima of 70, 100, and 90 nm, respectively. The albedos in those filters, reported as percentages, were 5.9 0.1 (*U*), 8.9 0.1 (*B*), and 17.0 0.2 (*V*). The albedo values of our samples MASC-2 and MASC-3 most closely match the value in the *B* filter, suggesting that they are the most representative of the Martian surface. MASC-4 exhibits the lowest value, due to its higher surface roughness, placing it below the *B* filter value and toward the darker end of the *U-B-V* sequence. In contrast, the brightness of MASC-1 exceeds the B filter value, moving toward the higher end of that same sequence, in line with its high compactness. These references to the *U-B-V* sequence are introduced exclusively to indicate the direction of these departures relative to the Martian *B*-band albedo, not as direct wavelength-to-wavelength comparisons. Good agreement was also found between the observed Martian albedo in the *R* band (700 nm) and the measured values for the MASC analogs at 640 nm (E. Frattin et al. 2025), indicating that MASC-4 remains a suitable analog at longer wavelengths. This suggests that the MASC-2, MASC-3, and MASC-4 samples are suitable Martian regolith analogs at visible wavelengths. These similarities support the use of our samples as representative of Martian soil.

### 5.2. Phase Reddening and Polarimetric Color

The results of the present work at 488 nm, combined with those obtained by E. Frattin et al. (2025) at 640 nm, provide the opportunity to study the phase dependence of the color and the polarimetric color of the Martian analog regolith samples. Usually, the color of asteroids (A. Betzler & O. de Sousa 2020; A. Alvarez-Candal 2024) is expressed in magnitudes as follows:

$$C(\alpha) = -2.5 \log \frac{F_{11}^{\lambda_2}(\alpha)}{F_{11}^{\lambda_1}(\alpha)} \quad (1)$$

where $\lambda_1 = 640$ nm and $\lambda_2 = 488$ nm. The color $C(\alpha)$ is a discrete parameter representing the reflectance difference between two spectral bands. Positive values of $C(\alpha)$ indicate

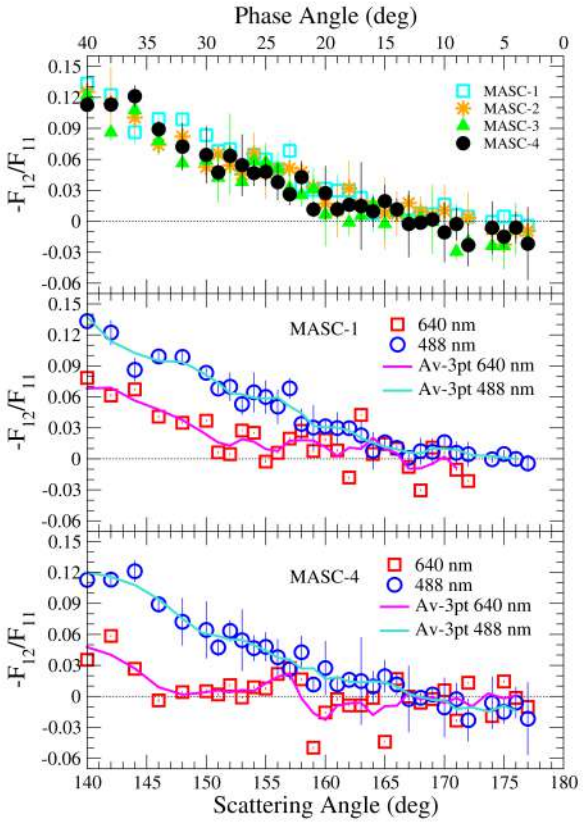


**Figure 7.** Backward region of DLP curves as functions of scattering (phase) angle, $\theta$ ($\alpha$). NPBs' behaviors under the effect of surface roughness at 488 nm (upper panel), and the effect of refractive index on MASC-1 and MASC-4 (middle and bottom panels, respectively) are shown. Turquoise and magenta curves are three-point moving averages for 488 and 640 nm, respectively

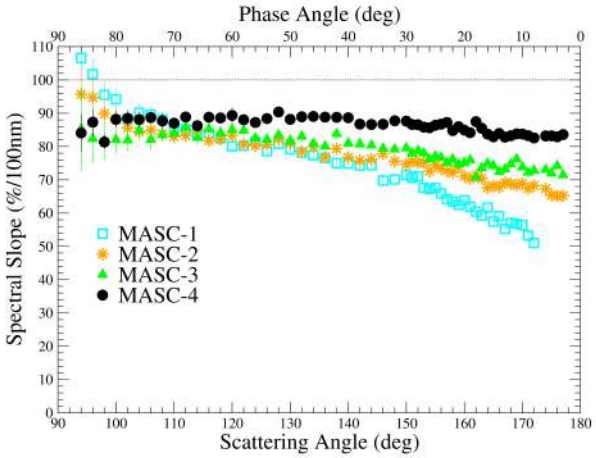


**Figure 8.** Spectral slopes as functions of scattering angle $\theta$ and phase angle $\alpha$ for each sample.

a reddish hue. The higher the value, the redder the sample. Negative values indicate a bluish hue. Regarding Figures 5 and 6, it is clear that our analog regoliths provide positive $C(\alpha)$ values, confirming their reddish color, which is expected given that the MMS2 powder appears red (J. Martikainen et al. 2023, 2025). In addition to color, we studied the phase reddening using spectral slopes (A. Delsanti et al. 2001; S. Spadaccia et al. 2023), defined as

**Table 3**
Linear Fitting Parameters for Spectral Slopes versus Phase Angle

| Samples | $a$ (%/100 nm deg) | | $b$ (%/100 nm) | |
|---|---|---|---|---|
| MASC-1 | 0.82 | 0.04 | 46.2 | 0.8 |
| MASC-2 | 0.38 | 0.02 | 64.0 | 0.4 |
| MASC-3 | 0.22 | 0.03 | 71.1 | 0.6 |
| MASC-4 | 0.17 | 0.02 | 81.9 | 0.4 |

**Note.** The phase angle interval for the fitting is between 3 and 30 .

$$\mathrm{SS}(\alpha) = \frac{F_{11}^{\lambda_1}(\alpha) - F_{11}^{\lambda_2}(\alpha)}{\lambda_1 - \lambda_2} \frac{2}{F_{11}^{\lambda_1}(\alpha) + F_{11}^{\lambda_2}(\alpha)} 10^4. \quad (2)$$

The spectral slopes are normalized to the mean value of the fluxes at each scattering angle and multiplied by $10^4$ to express them in %/100 nm. The spectral slope quantifies the rate of change of reflectance with wavelength. Figure 8 shows the spectral slopes for each sample as a function of the phase angle and the scattering angle. The spectral slope is obtained from the linear fit of the phase-function values as a function of wavelength at each scattering angle, whereas the color is defined as the logarithmic difference between the phase-function values at two distinct wavelengths. With only two wavelengths, the shapes of the color and spectral slope curves are similar. Positive spectral slope values indicate how red the spectrum of the samples is. All samples exhibit large spectral slopes across all scattering angles, consistent with the color results. Additionally, we find a correlation between spectral slope and surface roughness. To quantify phase reddening, we perform a linear regression of spectral slope versus phase angle. The results of the fit, obtained between 3 and 30 phase angles, are summarized in Table 3, where $a$ represents the slope and $b$ the extrapolated intercept at 0 .

Following E. Frattin et al. (2025), when the present rough surfaces are illuminated by a wide beam with normal incidence, surface roughness decreases the albedo while simultaneously promoting multiple scattering over single scattering. For smoother surfaces, conversely, the proportion of single to multiple scattering increases and, at the same time, the albedo increases. In order to understand the phase reddening results in Figure 8, together with the measured scattering matrices in Figures 5 and 6, the particle sizes and their clustering must be considered together with the surface roughness. Figures 1 and 2 suggest that the smoothest sample MASC-1 is composed of smaller particle clusters than the roughest sample MASC-4. In very rough samples, such as MASC-4, the phase functions at both wavelengths converge in shape, and the remaining differences are mainly due to the spectral dependence of the refractive index (upper-left panel of Figure 6). This can be understood by the large particle clusters and surface roughness having a uniform effect across the phase angle range. For MASC-1, the smoothest surface, $F_{11}(\alpha)$ shows a steeper slope at 488 nm than at 640 nm (upper-left panel of Figure 5), in agreement with increasing absorption for the former wavelength. The albedo of MASC-1 at 170 of scattering angle is considerably larger than that of MASC-4. The phase reddening for MASC-1 must relate to the spatial distribution of particles and their sizes, with absorption

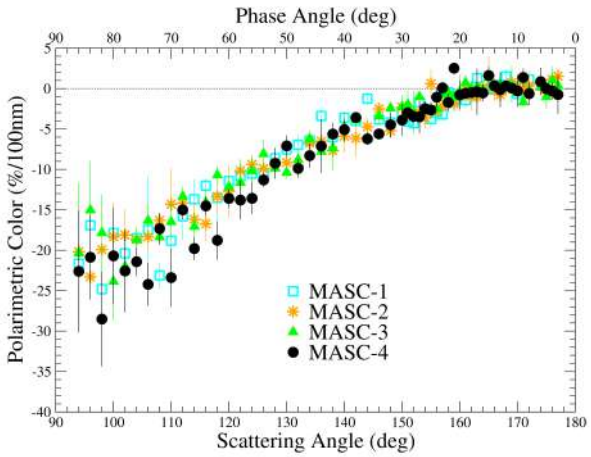


**Figure 9.** Polarimetric color as spectral slopes of the DLP as functions of scattering angle $\theta$ and phase angle $\alpha$ for each sample.

contrasts due to multiple interactions becoming more pronounced for larger phase angles.

Reddening has been studied by other authors. For example, P. Beck et al. (2012) measured meteorite reflectance between 450 and 650 nm and found higher reflectance at longer wavelengths within that range. S. Fornasier et al. (2020) studied the phase reddening of Bennu, obtaining low or negative values of the spectral slopes at very small phase angles. A. Alvarez-Candal (2024) and E. Wilawer et al. (2024) found that asteroids may either have reddening or bluing, and it may even occur that both effects are present in different phase angle intervals.

In our results, we observe the decrease in phase reddening with surface roughness (Table 3), but we do not capture a complex behavior as described by A. Alvarez-Candal (2024), as our measurements do not extend below 3 of phase angle. The values and shapes of our spectral slopes can be compared to asteroid taxonomic slopes (e.g., D. Perna et al. 2018). Based on curve shape alone, MASC-1 resembles X-type, MASC-4 resembles D-type (with the flattest dependence), and both MASC-2 and MASC-3 behave similar to S-types. Additionally, the NPB characteristics link our samples to both low-albedo classes (D, Ch) and even high-albedo (E), as reported by I. Belskaya et al. (2017). Nonetheless, our analogs cannot be unambiguously assigned to existing asteroid taxonomic classes.

Apart from the phase reddening, we investigated the role of absorption through the angular dependence of the polarimetric color (S. Bagnulo et al. 2025), defined as

$$\mathrm{PC}(\alpha) = \frac{|\mathrm{DLP}^{\lambda_1}(\alpha)| - |\mathrm{DLP}^{\lambda_2}(\alpha)|}{\lambda_1 - \lambda_2} 10^4 \qquad (3)$$

where $\mathrm{DLP}(\alpha) = -F_{12}(\alpha)/F_{11}(\alpha)$. The units of $\mathrm{PC}(\alpha)$ are the same as for the spectral slope, $\%/100$ nm. Positive and negative $\mathrm{PC}(\alpha)$ values indicate red and blue polarimetric color, respectively. Figure 9 shows the polarimetric color of our analog regolith samples as a function of phase angle (and scattering angle). Similar curves are obtained for all degrees of surface roughness, with no significant differences within the error bars. This behavior suggests that surface roughness does not noticeably affect the polarimetric color. Within the phase angle range from 3 to 20 , the $\mathrm{PC}(\alpha)$ values are distributed around the neutral level, gradually shifting toward blue at larger phase angles. This trend is explained by the stronger absorption at 488 nm compared to 640 nm, which dominates over any effect of surface roughness. Finally, the marked phase dependence of $\mathrm{PC}(\alpha)$ across a wide angular range suggests that this parameter can be a useful diagnostic of chemical composition. In contrast, measurements restricted to narrow phase angle intervals may not be representative of the overall behavior of the polarimetric color. These results may provide insights into how asteroids and comet nuclei polarize the light. Comets are surrounded by dust whose polarimetric response interferes and eclipses the comet nuclei (S. Bagnulo et al. 2025). This fact makes it easier observe asteroids than comet nuclei (I. Belskaya et al. 2005; S. Bagnulo et al. 2010; A. Cellino et al. 2018; E. Hadamcik et al. 2023; Y. G. Kwon et al. 2023), so experimental data become essential to interpret their scattering properties and to place the few existing measurements in a broader context.

### 5.3. Regolith Albedo versus Maximum DLP

The relationship between geometric albedo and the maximum DLP, known as Umov's law, is widely used in astronomy to characterize asteroid surfaces (E. Zubko et al. 2011, 2018; A. Cellino et al. 2015a; E. Hadamcik et al. 2023). Our experiments provide data to test Umov's law, as we obtain a proxy for the geometric albedo and the DLP curves. Although geometric albedo should ideally be measured at a phase angle of 0 (scattering angle of 180 ), our values at a phase angle of 10 (scattering angle of 170 ) can be used to evaluate Umov's law, since we are comparing relative differences among samples to identify trends.

Our albedo results, summarized in Table 2, exhibit two clear trends: (1) A decrease in albedo with increasing absorption. Our samples have a higher imaginary part of refractive index at 488 nm than at 640 nm, leading to stronger absorption in the blue and consequently lower scattering and albedo. (2) A decrease in albedo with increasing surface roughness. Surface roughness introduces pores and cavities that act as light traps. Rays undergo multiple interactions and are more likely to be absorbed or scattered weakly, reducing the net albedo.

The emerging question is whether these mechanisms also affect the DLP maximum. Due to our experimental geometry, we lack data beyond 90 phase angle, where similarly sized particles typically exhibit peak polarization (O. Muñoz et al. 2020). Therefore, our analysis is limited to the measured angular range.

As shown in Figure 4 (upper-middle panel), we do not find significant differences in the DLP maximum among the four samples. This suggests that the decrease in albedo due to surface roughness does not correspond to a change in the DLP maximum, in contradiction with Umov's law. This deviation is consistent with previous results obtained by E. Frattin et al. (2025) at 640 nm. In contrast, the effect of the refractive index (shown in the upper-middle panels of Figures 5 and 6) reveals a different trend. Regardless of surface roughness, a higher imaginary part of the refractive index leads to a clear increase in the DLP values, especially near 90 , where the DLP peak is expected. Thus, absorption via the imaginary refractive index does satisfy Umov's law within our angular range.

These results raise the question of whether surface morphology introduces deviations that cause Umov's law to fail. Other studies have also reported such anomalies. For instance, T. Ito et al. (2018) observed that asteroid Phaethon exhibits higher polarization relative to its albedo than expected. M. Zheltobryukhov et al. (2018) found that Phaethon's polarization-albedo values do not fit the lunar Umov diagram. Y. G. Kwon et al. (2023) reported that C-type asteroids do not display a clear inverse albedo-polarization correlation, whereas S-type asteroids generally follow Umov's law. For these reasons, our results remain intriguing and suggest that the albedo–DLP relationship is more complex than previously assumed. We also should note that Umov's law is by no means universal, and deviations from Umov's law can be attributed to particle size (Y. Shkuratov & N. Opanasenko 1992; Y. Shkuratov et al. 2025, 2026) and can be used to characterize the size of regolith constituents. Such research has been performed for lunar regolith (M. Jeong et al. 2018).

## 6. Summary and Conclusions

In this work, we present experimental light-scattering matrices at 488 nm for four regolith analog samples. All four were produced from the same powder but differ in surface roughness. These samples were previously studied at 640 nm by E. Frattin et al. (2025). All elements of the scattering matrix exhibit a strong wavelength dependence. The higher imaginary part of the refractive index at 488 nm leads to a decrease in sample albedo and an increase in the positive branch of the degree of linear polarization, while the NPB becomes weaker. Other scattering-matrix elements show reduced depolarizing effects as absorption increases. No significant differences are observed in the positive branch of the DLP across surface roughness. However, depolarizing effects in the $F_{22}(\theta)/F_{11}(\theta)$, $F_{33}(\theta)/F_{11}(\theta)$, and $F_{44}(\theta)/F_{11}(\theta)$ scattering-matrix elements become more pronounced with increasing surface roughness, while absorption introduces a polarizing effect in the same scattering-matrix elements.

Furthermore, we have studied the color and spectral slopes of our samples. The color values are consistent with the visually observed reddish-brown appearance of the regolith analogs. We also observe a decrease in spectral slopes with increasing scattering angle, indicating that our samples exhibit phase reddening. A clear trend is found between phase reddening and surface roughness: phase reddening is more pronounced for smoother surfaces and becomes nearly flat for very rough ones. Additionally, within our measured angular range, the absorption effect is consistent with Umov's law, while the effects of surface roughness do not appear to support its validity. Further studies are required to better isolate and understand the impact of physical properties on scattering behavior.

This study is part of an ongoing effort to investigate the scattering behavior of planetary regolith analogs. As a next step, we aim to examine millimeter-sized pebbles derived from the same bulk material used to produce the regolith samples analyzed here. A set of pebbles will be prepared by fragmenting the sintered aggregates, and the scattering matrix will be measured for each individual pebble. These forthcoming results will provide further insight into how chemical composition and morphology influence scattering behavior, contributing to the interpretation of remote observations of comets, asteroids, and other small solar system bodies.

## Acknowledgments

The authors acknowledge support from grant PID2021-123370OB-I00 and the Severo Ochoa grant CEX2021-001131-S, funded by MCIN/AEI/10.13039/501100011033. The authors also acknowledge support from grant PID2024-156713OB-I00 funded by MICIU/AEI/10.13039/501100011033. F.J.G.I. acknowledges support from grant PRE2022-103967 funded by MCIN/AEI/10.13039/501100011033. A.A.C. acknowledges support from grant PID2023-153123NB-I00 funded by MCIN/AEI/10.13039/501100011033. This project was also supported by the NASA KPLO Participating Scientist Program NNH18ZDA001N-KPLOPSP, grant 80NSSC21K0755. K.M. and A.P.'s research was supported by the Research Council of Finland grants Nos 336546, 345115, and 359893. The authors thank Rocío Márquez Crespo and Fátima Linares Ordóñez from the Scientific Instrumentation Center of the University of Granada for providing the SEM and AFM images, respectively.

## Data Availability

The experimental data are freely available at the Granada-Amsterdam Light Scattering Database, https://scattering.iaa.es/, under the request of citation of this paper and O. Muñoz et al. (2025).

## Author Contributions

F.J. García-Izquierdo: writing—original draft, review and editing, investigation, data curation, methodology, formal analysis, conceptualization, validation. E. Frattin: writing—review and editing, investigation, methodology, conceptualization, validation. J. Martikainen: writing—review and editing, validation. O. Muñoz: writing—review and editing, investigation, conceptualization, validation, supervision, resources, funding acquisition. A. Alvarez-Candal: writing—review and editing, conceptualization, validation. F. Moreno: writing—review and editing, conceptualization, validation. M. Passas-Varo: writing—review and editing, data curation, validation. J.C. Gómez-Martín: writing—review and editing, validation. T. Jardiel: writing—review and editing, methodology, resources, validation. M. Peiteado: writing—review and editing, methodology, resources, validation. A.C. Caballero: writing—review and editing, methodology, resources, validation. G. Videen: writing—review and editing, conceptualization, validation. J. Markkanen: writing—review and editing, conceptualization, validation. A. Penttilä: writing—review and editing, conceptualization, validation. K. Muinonen: writing—review and editing, conceptualization, validation.

## Appendix
## Other Experimental Scattering-matrix Elements

Figure A1 presents the angular dependence of the measured normalized off-diagonal elements $F_{13}/F_{11}$, $F_{14}/F_{11}$, $F_{24}/F_{11}$, $F_{31}/F_{11}$, and $F_{41}/F_{11}$ of the scattering matrix for the MASC samples at 488 nm, from 94 to 177 in scattering angle. For all MASC samples, these elements remain close to zero within the experimental uncertainties and do not exhibit any systematic dependence on scattering angle or roughness. This behavior indicates that cross-polarization effects associated with these matrix elements are negligible for the investigated surfaces under normal incidence.

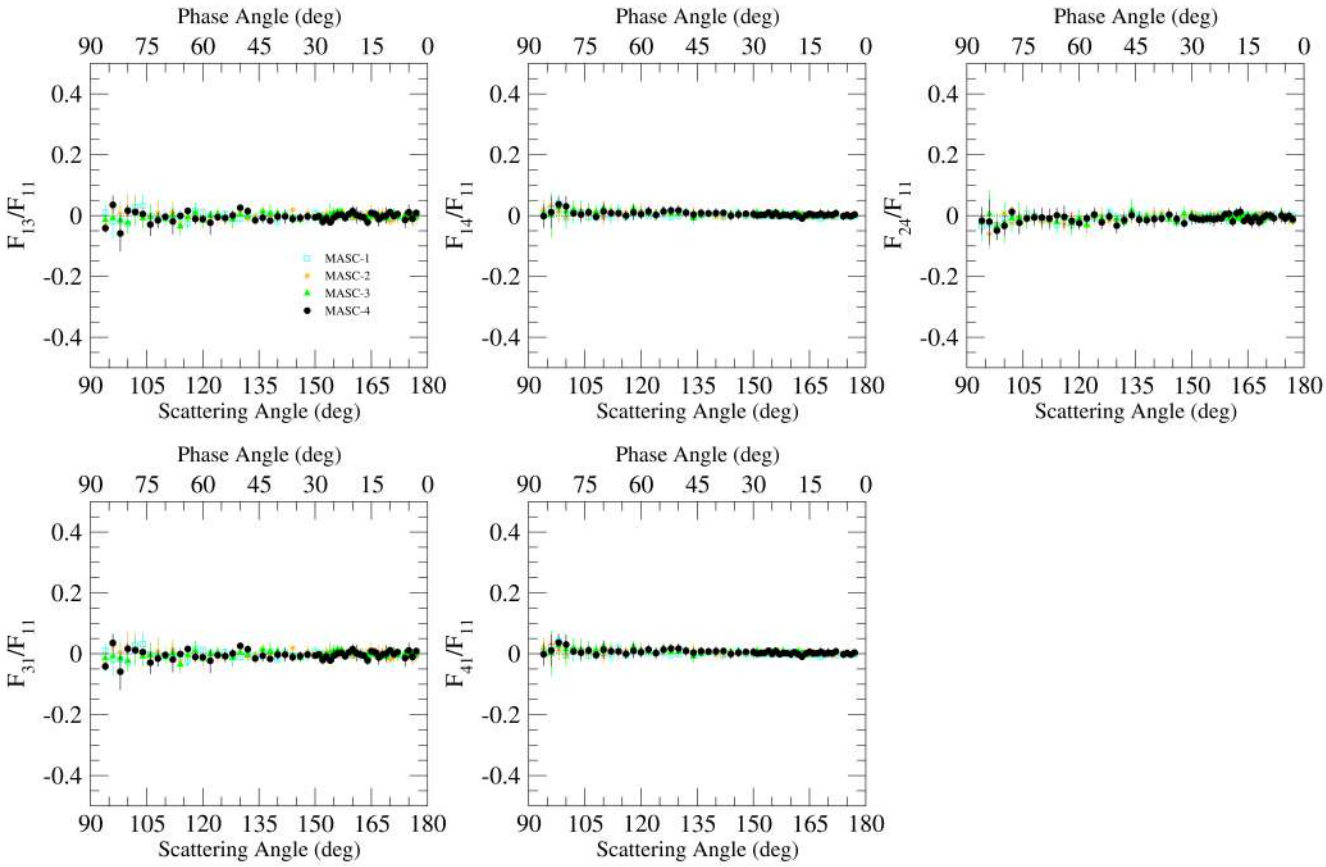


**Figure A1.** Experimental scattering-matrix elements as functions of the scattering (phase) angle, $\theta$ ($\alpha$), for MASC-1 (cyan empty squares), MASC-2 (orange stars), MASC-3 (green triangles), and MASC-4 (black circles). The wavelength is 488 nm.

## ORCID iDs

Francisco J. García-Izquierdo https://orcid.org/0000-0002-0246-4648
Elisa Frattin https://orcid.org/0000-0001-6428-4055
Julia Martikainen https://orcid.org/0000-0003-2211-4001
Olga Muñoz https://orcid.org/0000-0002-5138-3932
Alvaro Alvarez-Candal https://orcid.org/0000-0002-5045-9675
Fernando Moreno https://orcid.org/0000-0003-0670-356X
María Passas-Varo https://orcid.org/0000-0001-8546-1292
Juan Carlos Gómez-Martín https://orcid.org/0000-0001-7972-085X
Teresa Jardiel https://orcid.org/0000-0002-0163-7324
Marco Peiteado https://orcid.org/0000-0003-3510-6676
Amador C. Caballero https://orcid.org/0000-0002-0571-6302
Gorden Videen https://orcid.org/0000-0002-4177-7364
Johannes Markkanen https://orcid.org/0000-0001-5989-3630
Antti Penttilä https://orcid.org/0000-0001-7403-1721
Karri Muinonen https://orcid.org/0000-0001-8058-2642

## References

Alvarez-Candal, A. 2024, A&A, 685, A29
Bagnulo, S., Belskaya, I., Cellino, A., et al. 2025, A&ARv, 32, 7
Bagnulo, S., Cellino, A., & Sterzik, M. 2015, MNRAS: Letters, 446, L11
Bagnulo, S., Tozzi, G. P., Boehnhardt, H., Vincent, J.-B., & Muinonen, K. 2010, A&A, 514, A99
Beck, P., Pommerol, A., Thomas, N., et al. 2012, Icar, 218, 364
Belskaya, I., & Bagnulo, S. 2015, in Polarimetry of Stars and Planetary Systems, ed. L. Kolokolova, J. Hough, & A.-C. Levasseur-Regourd (Cambridge Univ. Press), 405
Belskaya, I., Fornasier, S., Tozzi, G., et al. 2017, Icar, 284, 30
Belskaya, I., Shkuratov, Y. G., Efimov, Y. S., et al. 2005, Icar, 178, 213
Betzler, A., & de Sousa, O. 2020, NewA, 75, 101320
Cellino, A., Bagnulo, S., Belskaya, I., & Christou, A. 2018, MNRAS: Letters, 481, L49
Cellino, A., Bagnulo, S., Gil-Hutton, R., et al. 2015a, MNRAS, 451, 3473
Cellino, A., Gil-Hutton, R., & Belskaya, I. 2015b, in Polarimetry of Stars and Planetary Systems, ed. L. Kolokolova, J. Hough, & A.-C. Levasseur-Regourd (Cambridge Univ. Press), 360
Cellino, A., Hutton, R. G., Di Martino, M., et al. 2005, Icar, 179, 304
Delsanti, A., Boehnhardt, H., Barrera, L., et al. 2001, A&A, 380, 347
Fornasier, S., Belskaya, I., Shkuratov, Y. G., et al. 2006, A&A, 455, 371
Fornasier, S., Hasselmann, P., Deshapriya, J. P., et al. 2020, A&A, 644, A142
Frattin, E., García-Izquierdo, F. J., Martikainen, J., et al. 2025, A&A, 697, A137
Frattin, E., Martikainen, J., Muñoz, O., et al. 2022, MNRAS, 517, 5463
Frattin, E., Muñoz, O., Moreno, F., et al. 2019, MNRAS, 484, 2198
Gadelmawla, E. S., Koura, M. M., Maksoud, T. M., Elewa, I. M., & Soliman, H. H. 2002, J. Mater. Process. Technol., 123, 133
Geem, J., Ishiguro, M., Takahashi, J., et al. 2022, MNRAS: Letters, 516, L53
Gómez-Martín, J. C., Guirado, D., Frattin, E., et al. 2021, JQSRT, 271, 107761
Gómez-Martín, J. C., Muñoz, O., Martikainen, J., et al. 2023, ApJS, 270, 2
Hadamcik, E., Renard, J.-B., Lasue, J., Levasseur-Regourd, A. C., & Ishiguro, M. 2023, MNRAS, 520, 1963
Hadamcik, E., Renard, J.-B., Levasseur-Regourd, A. C., & Lasue, J. 2011, in Polarimetric Detection, Characterization and Remote Sensing, ed. M. I. Mishchenko et al. (Springer), 137
Hansen, J. E., & Travis, L. D. 1974, SSRv, 16, 527
Hovenier, J. W., Van der Mee, C. V., & Domke, H. 2004, Transfer of Polarized Light in Planetary Atmospheres: Basic Concepts and Practical Methods (Springer)
Ishiguro, M., Kuroda, D., Watanabe, M., et al. 2017, AJ, 154, 180

Ito, T., Ishiguro, M., Arai, T., et al. 2018, NatCo, 9, 2486
Jeong, M., Choi, Y.-J., Kim, S. S., et al. 2018, ApJ, 869, 67
Kuroda, D., Ishiguro, M., Watanabe, M., et al. 2018, A&A, 611, A31
Kwon, Y. G., Bagnulo, S., & Cellino, A. 2023, A&A, 677, A146
Mallama, A. 2007, Icar, 192, 404
Markkanen, J., & Penttilä, A. 2023, JQSRT, 310, 108733
Martikainen, J., Muñoz, O., Gómez Martín, J. C., et al. 2025, MNRAS, 537, 1489
Martikainen, J., Muñoz, O., Jardiel, T., et al. 2023, ApJS, 268, 47
Muinonen, K., Leppälä, A., & Markkanen, J. 2025, JQSRT, 330, 109226
Muinonen, K., Markkanen, J., Väisänen, T., Peltoniemi, J., & Penttilä, A. 2018, OptL, 43, 683
Muinonen, K., Mishchenko, M., Dlugach, J., et al. 2012, ApJ, 760, 118
Muñoz, O., Frattin, E., Jardiel, T., et al. 2021, ApJS, 256, 17
Muñoz, O., Moreno, F., Gómez-Martín, J. C., et al. 2020, ApJS, 247, 19
Muñoz, O., Moreno, F., Guirado, D., et al. 2010, JQSRT, 111, 187
Muñoz, O., Moreno, F., Guirado, D., et al. 2011, Icar, 211, 894
Muñoz, O., Frattin, E., Martikainen, J., et al. 2025, JQSRT, 331, 109252
Nelson, R. M., Boryta, M. D., Hapke, B. W., et al. 2018, Icar, 302, 483
Ovcharenko, A. A., Bondarenko, S. Y., Zubko, E. S., et al. 2006, JQSRT, 101, 394
Penttilä, A., Markkanen, J., Väisänen, T., et al. 2021, JQSRT, 262, 107524
Perna, D., Barucci, M. A., Fulchignoni, M., et al. 2018, P&SS, 157, 82
Poch, O., Cerubini, R., Pommerol, A., Jost, B., & Thomas, N. 2018, JGRE, 123, 2564
Sanchez, J. A., Reddy, V., Nathues, A., et al. 2012, Icar, 220, 36
Shkuratov, Y., Bondarenko, S., Ovcharenko, A., et al. 2006, JQSRT, 100, 340
Shkuratov, Y., & Opanasenko, N. 1992, Icar, 99, 468
Shkuratov, Y., Kaydash, V., Head, J., et al. 2026, Icar, 444, 116796
Shkuratov, Y., Videen, G., & Kaydash, V. 2025, Optics of the Moon (1st ed.; Elsevier)
Spadaccia, S., Patty, C., Capelo, H. L., Thomas, N., & Pommerol, A. 2022, A&A, 665, A49
Spadaccia, S., Patty, C. L., Thomas, N., & Pommerol, A. 2023, Icar, 396, 115503
Stankevich, D., Shkuratov, Y., Sim, C. K., et al. 2023, JQSRT, 296, 108457
Tatsumi, E., Domingue, D., Schröder, S., et al. 2020, A&A, 639, A83
Thompson, W. 2015, Icar, 261, 122
van de Hulst, H. C. 1981, Light Scattering by Small Particles (Dover)
Wilawer, E., Muinonen, K., Oszkiewicz, D., Kryszczyńska, A., & Colazo, M. 2024, MNRAS, 531, 2802
Zheltobryukhov, M., Chornaya, E., Kochergin, A., et al. 2018, A&A, 620, A179
Zubko, E., Chornaya, E., Zheltobryukhov, M., et al. 2020, Icar, 336, 113453
Zubko, E., Videen, G., Shkuratov, Y., Muinonen, K., & Yamamoto, T. 2011, Icar, 212, 403
Zubko, E., Videen, G., Zubko, N., & Shkuratov, Y. 2018, MNRAS, 477, 4866